Magnetic Resonance Imaging 60 (2019) 145–156

Contents lists available at ScienceDirect

Magnetic Resonance Imaging

journal homepage: www.elsevier.com/locate/mri

Original contribution

Compressed sensing reconstruction of 7 Tesla ^{23}Na multi-channel breast data using ^{1}H MRI constraint

Sebastian Lachner[a,*], Olgica Zaric[b], Matthias Utzschneider[a], Lenka Minarikova[b], Štefan Zbýň[b,c], Bernhard Hensel[d], Siegfried Trattnig[b], Michael Uder[a], Armin M. Nagel[a,e,f]

[a] Institute of Radiology, University Hospital Erlangen, Friedrich-Alexander-Universität Erlangen-Nürnberg (FAU), Erlangen, Germany
[b] High Field MR Center, Department of Biomedical Imaging and Image-guided Therapy, Medical University of Vienna, Vienna, Austria
[c] Center for Magnetic Resonance Research, Department of Radiology, University of Minnesota, Minneapolis, MN, USA
[d] Center for Medical Physics and Engineering, Friedrich-Alexander-Universität Erlangen-Nürnberg (FAU), Erlangen, Germany
[e] Division of Medical Physics in Radiology, German Cancer Research Centre (DKFZ), Heidelberg, Germany
[f] Institute of Medical Physics, Friedrich-Alexander-Universität Erlangen-Nürnberg (FAU), Erlangen, Germany

ARTICLE INFO

Keywords:
Sodium (^{23}Na) breast MRI
7 Tesla
Iterative reconstruction
Compressed sensing (CS)
Multi-channel
Prior knowledge

ABSTRACT

Purpose: To reduce acquisition time and to improve image quality in sodium magnetic resonance imaging (^{23}Na MRI) using an iterative reconstruction algorithm for multi-channel data sets based on compressed sensing (CS) with anatomical ^{1}H prior knowledge.

Methods: An iterative reconstruction for ^{23}Na MRI with multi-channel receiver coils is presented. Based on CS it utilizes a second order total variation (TV$^{(2)}$), adopted by anatomical weighting factors (AnaWeTV$^{(2)}$) obtained from a high-resolution ^{1}H image. A support region is included as additional regularization. Simulated and measured ^{23}Na multi-channel data sets (n = 3) of the female breast acquired at 7 T with different undersampling factors (USF = 1.8/3.6/7.2/14.4) were reconstructed and compared to a conventional gridding reconstruction. The structural similarity was used to assess image quality of the reconstructed simulated data sets and to optimize the weighting factors for the CS reconstruction.

Results: Compared with a conventional TV$^{(2)}$, the AnaWeTV$^{(2)}$ reconstruction leads to an improved image quality due to preserving of known structure and reduced partial volume effects. An additional incorporated support region shows further improvements for high USFs. Since the decrease in image quality with higher USFs is less pronounced compared to a conventional gridding reconstruction, proposed algorithm is beneficial especially for higher USFs. Acquisition time can be reduced by a factor of 4 (USF = 7.2), while image quality is still similar to a nearly fully sampled (USF = 1.8) gridding reconstructed data set.

Conclusion: Especially for high USFs, the proposed algorithm allows improved image quality for multi-channel ^{23}Na MRI data sets.

1. Introduction

Sodium ions (Na^+) play an important role in cellular metabolic processes. The sodium-potassium pump (3 Na^+/2 K^+-ATPase) ensures a sodium concentration gradient between the intra- and extracellular compartment: against the electrochemical gradient potassium-ions are transported in and sodium-ions out of the cell. Thus, in healthy tissue, the extracellular sodium concentration is approximately ten-fold higher compared with the intracellular concentration. A changed tissue sodium concentration refers to altered metabolic processes and occurs in diseases such as stroke [1,2], multiple sclerosis [3–5] and cancer [6,7]. For example, breast cancer shows significantly increased sodium concentration compared to glandular or fatty tissue [8–10].

Sodium (^{23}Na) magnetic resonance imaging (MRI) offers the possibility to quantify the Na^+ concentration non-invasively [11,12]. Due to low in vivo sodium concentration, low MR sensitivity and significantly shorter relaxation times, ^{23}Na MRI suffers from an inherently low signal-to-noise ratio (SNR). As a consequence, the spatial resolution is limited and image quality is affected by artifacts, such as partial volume effects or Gibbs ringing. However, different hardware and software developments have been proposed to overcome these restrictions and to enhance image quality. One possibility is to increase the magnetic field

* Corresponding author at: Institute of Radiology, University Hospital Erlangen, Friedrich-Alexander-Universität Erlangen-Nürnberg (FAU), Maximiliansplatz 3, 91054 Erlangen, Germany.
E-mail address: sebastian.lachner@uk-erlangen.de (S. Lachner).

https://doi.org/10.1016/j.mri.2019.03.024
Received 10 December 2018; Received in revised form 1 March 2019; Accepted 29 March 2019

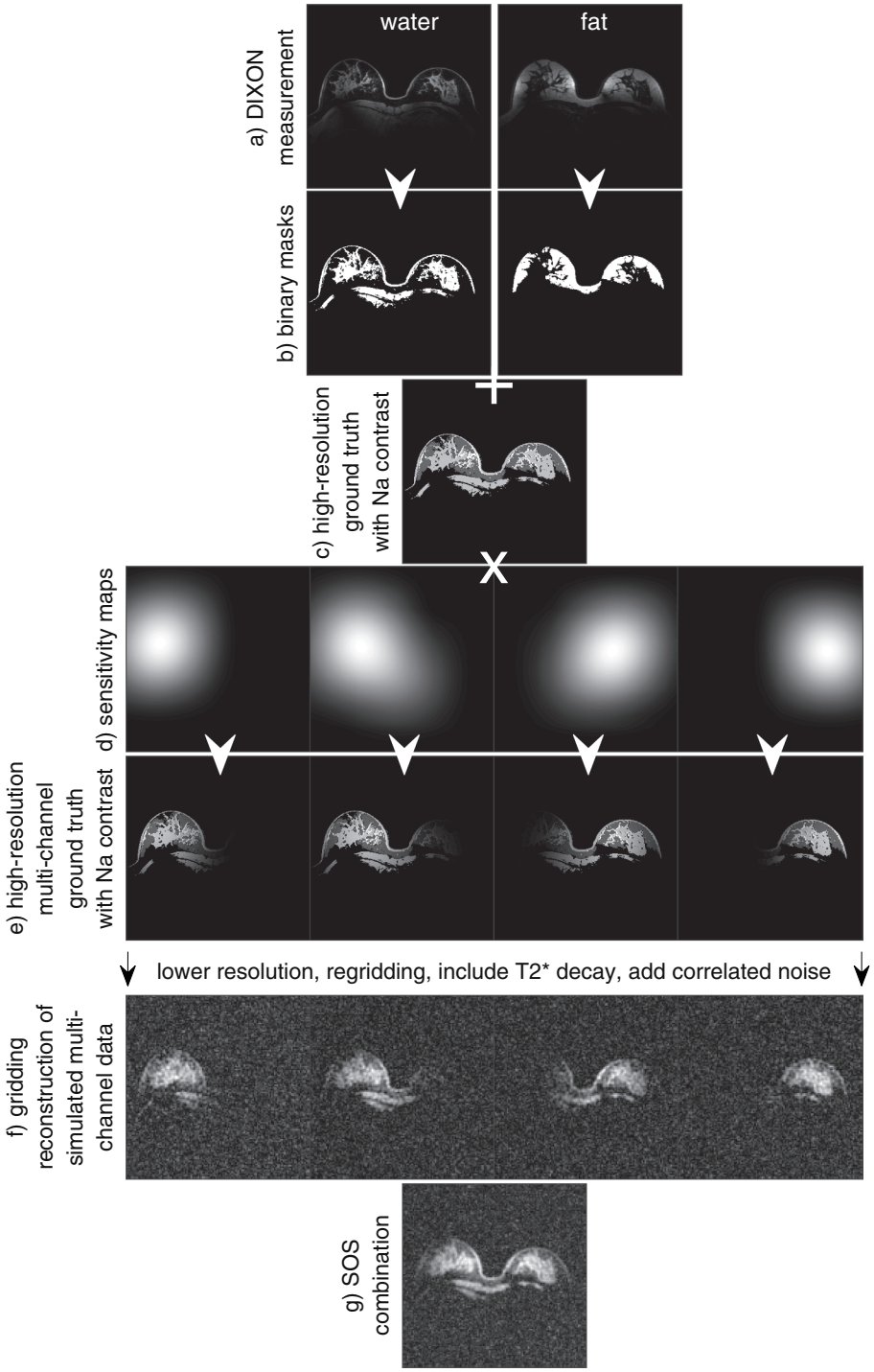

Fig. 1. Simulation scheme of a ^{23}Na MRI radial multi-channel data set. A high-resolution ^{1}H Dixon measurement (a) was employed to generate fat and water binary masks (BMs) (b). The BMs were multiplied by weighting factors (2.5 for the water BM and 1.0 for the fat BM) and summed up to gain a high-resolution ^{23}Na MRI ground truth data set (FOV: $(320\,\mathrm{mm})^3$, nominal resolution: $(1\,\mathrm{mm})^3$) (c). By multiplying the high-resolution ground truth with sensitivity maps (4 out of 14 are shown) (d) a high-resolution multi-channel ground truth was obtained (e). The resolution of this Cartesian data set was reduced to $(3\,\mathrm{mm})^3$, regridded to the radial trajectory (here: 20.000 projections, 384 radial samples), T_2^* decay of ^{23}Na signal and correlated noise were added. Gridding reconstruction of the simulated radial multi-channel data set (FOV: $(320\,\mathrm{mm})^3$, reconstructed to $(2.5\,\mathrm{mm})^3$ via zero filling) (f) and the corresponding SOS combination (g). This scheme can be used to simulate any arbitrary ^{23}Na radial data set and to test the algorithm.

strength to improve SNR [13]. Furthermore, advanced image acquisition pulse sequences [14] such as 3D density-adapted radial [15], continuously oscillating gradients [16], 3D cones [17], twisted projection imaging [18,19] or FLORET [20] enable efficient k-space sampling and ultra-short echo times. This is a prerequisite for SNR efficient ^{23}Na MRI due to short transverse relaxation times of the ^{23}Na nucleus [21]. In addition, multi-channel receive array coils can be used to improve SNR [22–24]. Furthermore, sophisticated techniques such as compressed sensing (CS) [25] can be applied for image reconstruction. However, CS and related iterative image reconstruction techniques are still rarely used in ^{23}Na MRI, although they can yield significant improvement in image quality or reduce acquisition time [26–28]. MR images of the same body region acquired with different MRI contrasts are highly correlated. Especially for known tissue boundaries, such as between fat and glandular tissue in the breast, information from high-resolution ^{1}H images can be incorporated – e.g. by locally adapting the weighting factors of the CS reconstruction. This approach can further improve image quality and reduce partial volume effects [29]. If a multi-channel receive array is used [30], data from the separate channels needs to be combined. In low SNR applications, such as ^{23}Na MRI, a basic sum-of-square (SOS) combination leads to an amplification of the noise level in dark image regions [31]. Thus, more sophisticated methods such as adaptive combination (ADC) [31,32] or sensitivity encoding (SENSE) [33,34] can be used to optimally combine multi-

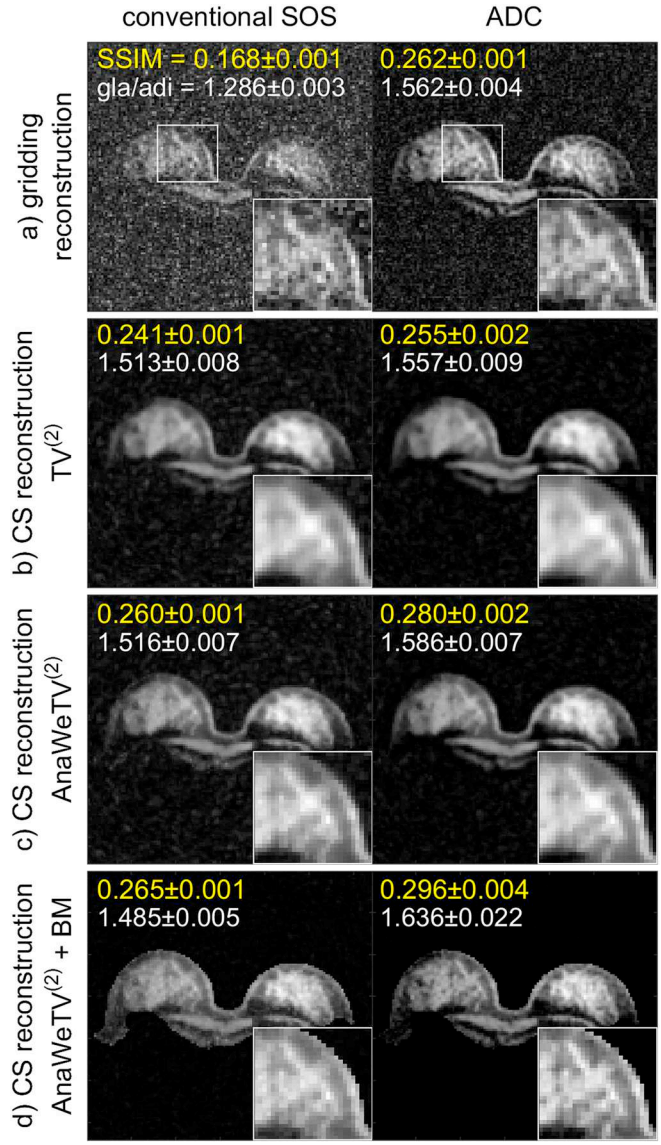

Fig. 2. Two different multi-channel combination methods (SOS and ADC) were applied to the simulated data set with 5000 projections (USF = 7.2) without raw data averaging. The mean SSIM values and the mean signal ratios for glandular/adipose tissue with standard deviations are indicated. a) Gridding reconstruction versus CS reconstruction with a $TV^{(2)}$ (b) and an $AnaWeTV^{(2)}$ (c) as sparsity transformation and an additional BM constraint (d). For the gridding reconstruction, the incorporation of noise correlations between the channels using ADC, leads to a clear improvement of the image quality, indicated by an increased SSIM value and ratio. For the CS reconstruction this difference is less pronounced. Using ADC (right column), the differences between the gridding and the CS reconstruction are less distinct compared to a conventional SOS reconstruction (left column). However, using the $AnaWeTV^{(2)}$ sparsity transformation with and without a BM, the CS reconstruction improves image quality.

channel coil array data.

So far, CS reconstruction and incorporation of prior knowledge have not been applied to multi-channel ^{23}Na MRI data. CS has been applied to 1-channel ^{23}Na MRI of human brain [26,27,29,35] and cartilage [28] only. In this work, a CS based reconstruction that incorporates prior knowledge with different subsequent multi-channel combination methods is presented. The performance of the applied methods was evaluated in simulations and in vivo ^{23}Na MRI measurements of the healthy female breast acquired at 7 T using a 14-channel phased array ^{23}Na/^{1}H coil.

2. Methods

2.1. Image reconstruction

The image reconstruction is based on the concept of CS [25]. A second order total variation ($TV^{(2)}$) is employed as sparsity transformation, which works as a conventional denoising technique [36,37]:

$$R_{TV^{(2)}}(x) = \sum_{\alpha \in \dim(x)} (\lambda \, \|D_\alpha^{(1)} x\|_1 + (1-\lambda)\|D_\alpha^{(2)} x\|_1). \tag{1}$$

Here, x represents the image vector and λ the weighting towards the first- $D_\alpha^{(1)}$ and second-order derivative $D_\alpha^{(2)}$ calculated in the direction α; λ is chosen to $\lambda = 0.77$ [36]. As proposed by Gnahm et al. [29] the $TV^{(2)}$ is adopted by anatomical weighting factors W_α ($AnaWeTV^{(2)}$):

$$R_{AnaWeTV^{(2)}}(x) = \sum_{\alpha \in \dim(x)} (\lambda \, \|W_\alpha D_\alpha^{(1)} x\|_1 + (1-\lambda)\|W_\alpha D_\alpha^{(2)} x\|_1). \tag{2}$$

For $(W_\alpha)_{ii} < 1$ the $TV^{(2)}$ is locally reduced, which preserves known tissue boundaries at the cost of locally reduced denoising. The entries $(W_\alpha)_{ii}$ of the diagonal matrix W_α are calculated from a registered and normalized high-resolution ^{1}H image r. Thereby, the presence of tissue boundaries is detected by calculating the first derivative

$$c_{\alpha,i} = (D_\alpha^{(1)} r)_i. \tag{3}$$

By inverting the confidence c_α and setting a sensible control parameter w_{max} to specify the amount of included prior information

$$w_{\alpha,i} = \min\{(c_{\alpha,i})^{-1}, w_{max}\}, \tag{4}$$

the final weighting factors are calculated via

$$(W_\alpha)_{ii} = \begin{cases} 0.1\dfrac{w_{\alpha,i} - \min(w_\alpha)}{w_{max} - \min(w_\alpha)} & for \quad w_{\alpha,i} < w_{max} \\ 1 & for \quad w_{\alpha,i} = w_{max} \end{cases}. \tag{5}$$

The anatomical prior information for the reconstruction of simulated data sets was obtained from the Dixon water binary mask (see Section 2.3); for the reconstruction of measured data sets from the Dixon water image (see Section 2.4). This ensures the incorporation of actual existing tissue boundaries, which can differ due to the thresholding step creating the binary mask. Since both images have different intensity ranges, the mean maximal derivative of the Dixon water binary mask is twice as high as of the Dixon water image. Therefore, w_{max} was chosen to $w_{max} = 20$ for measured data and to $w_{max} = 10$ for simulated data. This ensures that in both cases the amount of included prior information was similar. Thus, the $AnaWeTV^{(2)}$ works as a denoising technique whereas known tissue boundaries are preserved.

A support region, which matches the object shape [27], is included as additional, albeit simple regularizing prior information. The support region is obtained from the registered high-resolution ^{1}H image via appropriate closing and thresholding. It results in a binary mask (BM), which is 0 inside and 1 outside of the object. The BM is incorporated into the reconstruction as a further regularization by multiplying the current image x and the BM and summing up the elements:

$$R_{BM}(x) = \|BM \cdot x\|_2^2. \tag{6}$$

The BM regularization does not incorporate information about existing structure but information about noise and artifacts outside of the breast. However, by minimizing the BM regularization term noise and undersampling artifacts are suppressed, which in reverse helps to find a better solution of the underdetermined reconstruction problem. Therefore, an incorporated BM can improve image quality [27].

Image reconstruction is conducted via a CS scheme [25]. An objective function

$$f(x) = \frac{1}{2} \|Ax - y\|_2^2 + \sum_i \tau_i R_i(x) \tag{7}$$

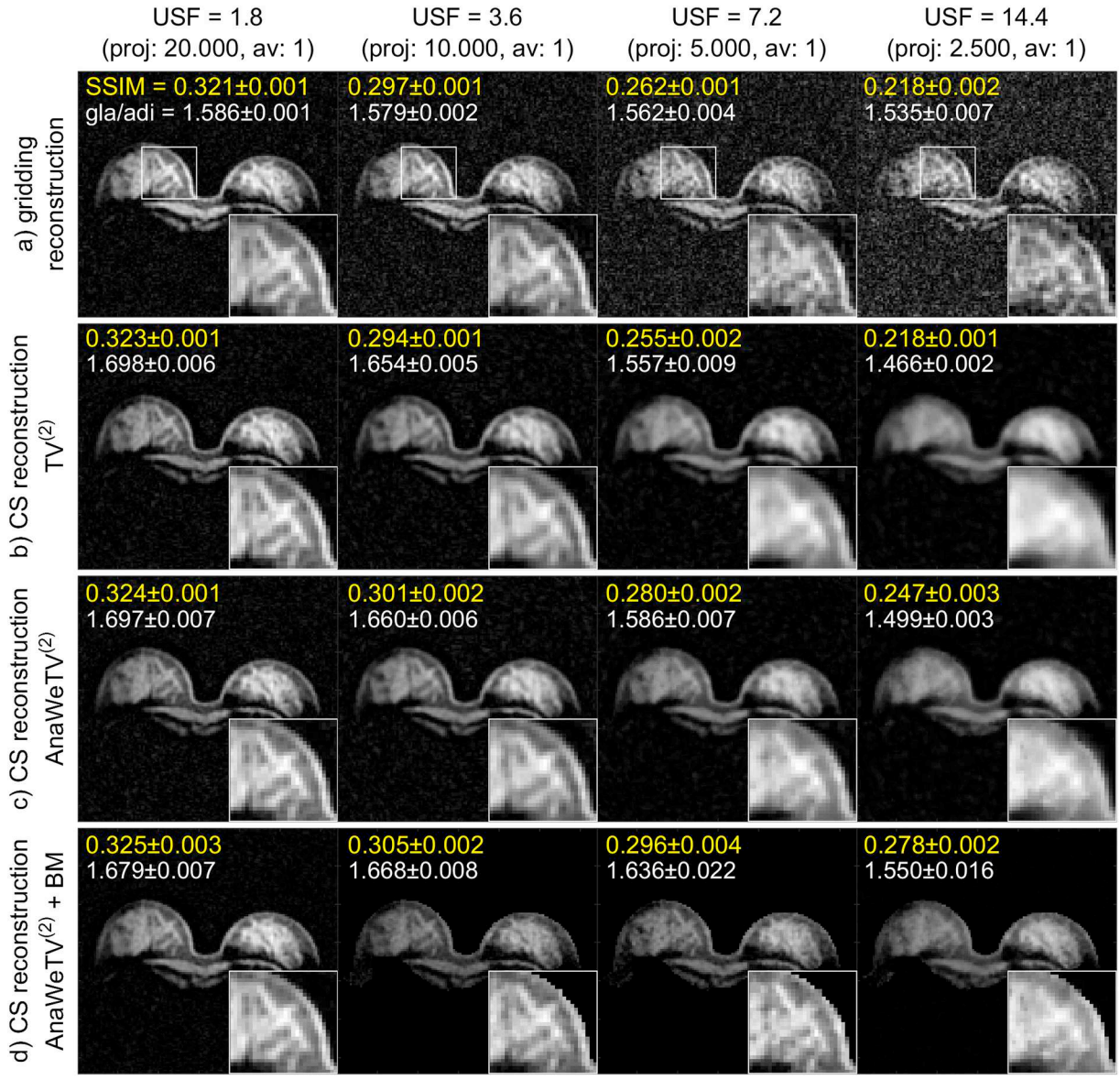

Fig. 3. Reconstruction of simulated multi-channel breast data with different USFs without raw data averaging, combined via ADC. The mean SSIM values and the mean signal ratios for glandular/adipose tissue with standard deviations are indicated. a) Gridding reconstruction versus CS reconstruction with a $TV^{(2)}$ (b) and an $AnaWeTV^{(2)}$ (c) as sparsity transformation and an additional BM constraint (d). The gridding reconstruction and the $TV^{(2)}$ CS reconstruction lead to similar results. However, especially for high USFs, the $AnaWeTV^{(2)}$ reconstruction with and without a BM shows its benefits and leads to an improved image quality. Despite undersampling image quality is preserved, using the CS reconstruction. Measurement time can be reduced (e.g. 4-fold), while obtaining results much closer to the nearly full-sampled gridding reconstructed data set than using the conventional gridding reconstruction.

is minimized through an iterative algorithm using the conjugate gradient method [38]. Here, A is the system matrix, which describes the imaging process and consists of a Fourier transformation followed by Kaiser-Bessel-Gridding to the radial k-space trajectory [39]. Thus, the first term ensures data consistency by calculating the difference between the raw data y and the current image vector x; the second term represents the regularizations. Via τ_i the data consistency and the regularization terms can be weighed against each other. The stopping criterion for the iterative algorithm is $\frac{\|x_{k+1}-x_k\|_2}{\|x_{k+1}\|_2} < 10^{-6}$ ten times in sequence. I.e. the algorithm stops if the relative change of the image x between two iterations is lower than 10^{-6} ten times in a row. If this is not reached within 300 iterations, the algorithm is stopped manually. To reconstruct multi-channel data sets, the depicted algorithm is parallelized using the OpenMP application programming interface [40]. The reconstructed multi-channel data set is subsequently combined (see Section 2.2).

The depicted $AnaWeTV^{(2)}$ and BM regularization is compared with a conventional $TV^{(2)}$ regularization and the gridding reconstruction [39] for ^{23}Na MRI of the female breast. The following reconstructions were applied and compared with each other:

a) A conventional gridding reconstruction.
b) An iterative CS reconstruction with a $TV^{(2)}$ regularization:

$$f(x) = \frac{1}{2}\|Ax - y\|_2^2 + \tau_{TV^{(2)}} \sum_{\alpha \in \dim(x)} (\lambda \|D_\alpha^{(1)} x\|_1 + (1-\lambda)\|D_\alpha^{(2)} x\|_1) \tag{7.1}$$

c) An iterative CS reconstruction with an $AnaWeTV^{(2)}$ regularization:

$$f(x) = \frac{1}{2}\|Ax - y\|_2^2 + \tau_{AnaWeTV^{(2)}} \sum_{\alpha \in \dim(x)} (\lambda \|W_\alpha D_\alpha^{(1)} x\|_1 + (1-\lambda)\|W_\alpha D_\alpha^{(2)} x\|_1) \tag{7.2}$$

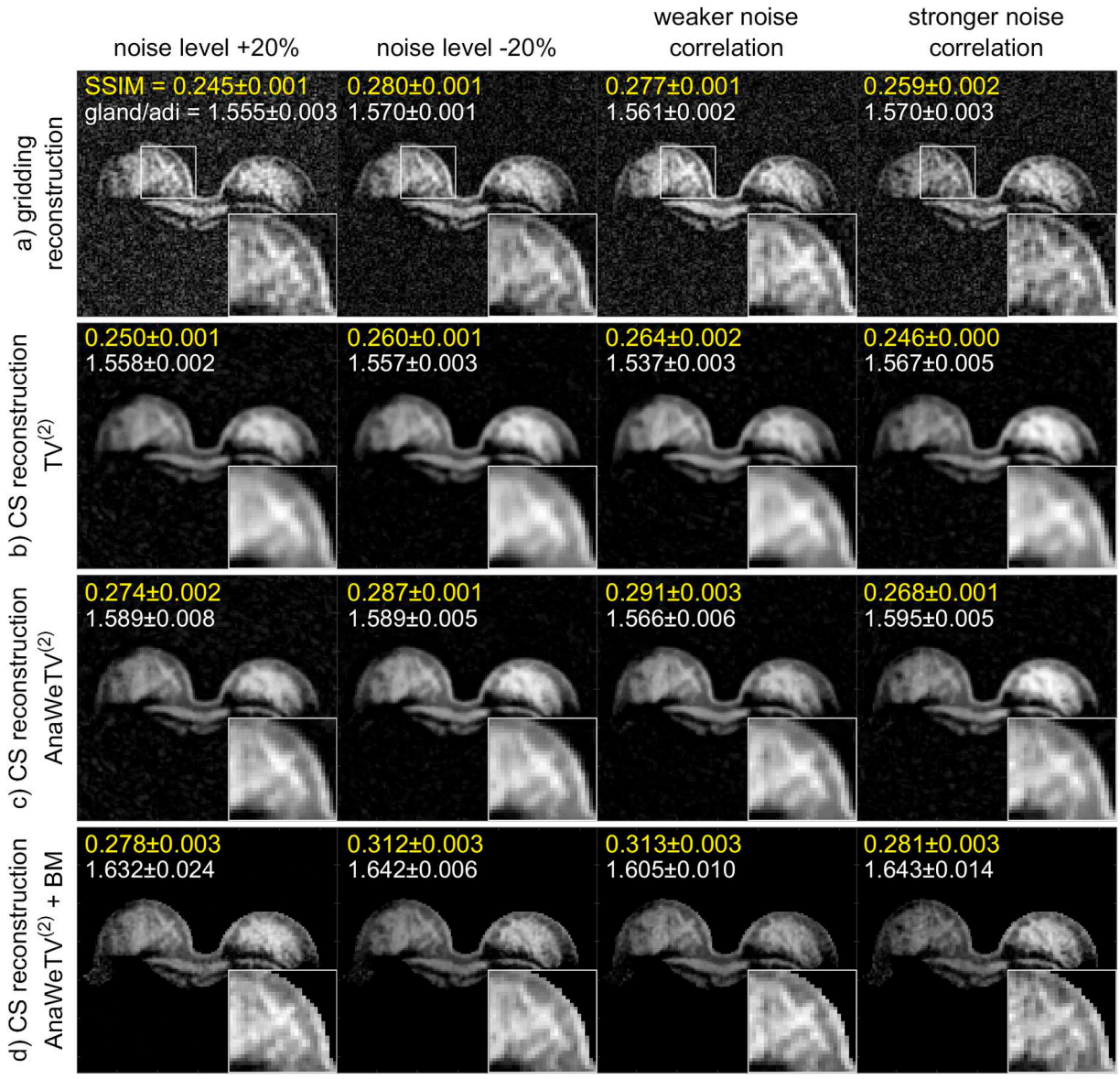

Fig. 4. Reconstruction of simulated multi-channel breast data with 5000 projections (USF = 7.2) with varied noise properties, without raw data averaging. a) Gridding reconstruction versus CS reconstruction with a $TV^{(2)}$ (b) and an $AnaWeTV^{(2)}$ (c) as sparsity transformation and an additional BM constraint (d). From the left to the right: noise level increased by 20%, noise level decreased by 20%, weaker and stronger noise correlations between the channels. The mean SSIM values and the mean signal ratios for glandular/adipose tissue with standard deviations are indicated. For the gridding as well as the CS reconstructions, the SSIM values are lower for the reconstructed data set with raised noise level or stronger noise correlation and higher for the data set with reduced noise level or weaker noise correlation with respect to the simulated data set matching the in vivo measurement (Fig. 3, second column from the right). For all assumed different noise properties, the $AnaWeTV^{(2)}$ + BM reconstruction performs best and increases the image quality compared to the ADC gridding reconstruction indicated by higher SSIM values and ratios.

d) An iterative CS reconstruction with an $AnaWeTV^{(2)}$ and an additional BM regularization:

$$f(x) = \frac{1}{2}\,\|Ax - y\|_2^2 + \tau_{\mathrm{AnaWeTV}^{(2)}} \sum_{\alpha \in \dim(x)} (\lambda\,\|W_\alpha D_\alpha^{(1)} x\|_1 + (1-\lambda)\|W_\alpha D_\alpha^{(2)} x\|_1) + \tau_{\mathrm{BM}}\,\|\mathrm{BM}\cdot x\|_2^2 \tag{7.3}$$

The reconstructions were executed on a desktop computer (Intel Core i7-6900K CPU @ 3.20 GHz, 64 GB RAM). The total CS reconstruction times depend on the data set and on the chosen regularization. For the 14-channel data set with 5.000 projections and an $AnaWeTV^{(2)}$ regularization, an approximate reconstruction time is 100 min.

2.2. Multi-channel combination

A conventional SOS [30] as well as ADC [31,32] was implemented to combine the reconstructed multi-channel data. The ADC algorithm was applied with a block size of 10 pixels and an interpolation factor of 2 pixels (resulting in an overlap of 8 pixels). Thereby an optimal weighting factor for each pixel is determined and applied locally. The noise covariance matrix, which describes the mutual coupling of the individual channels, was determined via a pre noise calibration scan.

2.3. Simulations

Dixon ^{1}H MRI water and fat images (FOV: 246x320x128 mm^3, nominal resolution: $(1\,mm)^3$, TR = 7.70 ms, TE_1 = 1.53 ms,

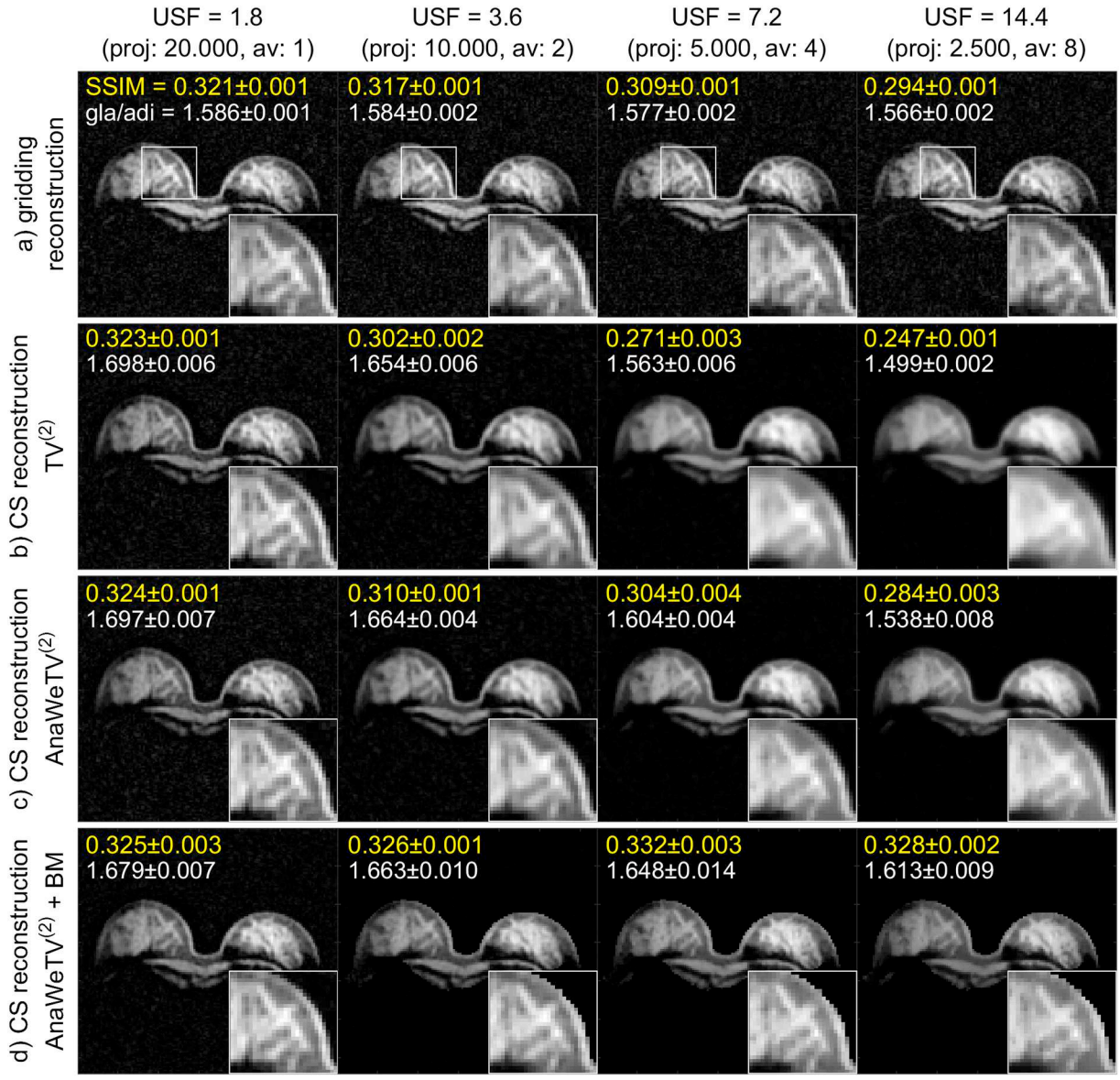

Fig. 5. Reconstruction of simulated multi-channel breast data with different USFs and raw data averaging, combined via ADC. The mean SSIM values and the mean signal ratios for glandular/adipose tissue with standard deviations are indicated. The number of averages was adjusted to keep the total acquisition time constant for different USFs. a) Conventional gridding reconstruction versus CS reconstruction with a $TV^{(2)}$ (b) and an $AnaWeTV^{(2)}$ (c) as sparsity transformation and an additional BM constraint (d). For the gridding, $TV^{(2)}$ and $AnaWeTV^{(2)}$ CS reconstructions, image quality decreases with higher USFs indicated by lower SSIM values and ratios. However, the decline is less pronounced compared to non-averaged raw data in Fig. 3. By incorporating the BM as additional regularization the image quality is similar for all USFs.

TE_2 = 3.06 ms, T_{AQ} = 1:46 min; Fig. 1a) were used to generate an artificial ^{23}Na MRI data set. Water/fat binary masks (BM_{water}/BM_{fat}), which are 1 inside the water/fat region and 0 everywhere else, were created by thresholding water/fat Dixon images (Fig. 1b). The masks were multiplied with weighting factors (2.5 for water mask, i.e. mainly glandular tissue and 1 for fat mask tissue) and added to gain a high-resolution 1-channel ground truth with ^{23}Na contrast: ^{23}Na 1-channel ground truth = $2.5 \cdot BM_{water} + 1 \cdot BM_{fat}$ (Fig. 1c). The ratio of 2.5 was based on previously published work [9], which reported a mean ratio between glandular and adipose tissue in breast of 2.5 (with a standard deviation of 1.35). To simulate a multi-channel ground truth, sensitivity maps were obtained by performing an uncombined gridding reconstruction of the nearly fully sampled measured data set (undersampling factor USF = 1.8) and dividing each single channel image by the SOS image. The sensitivity maps were further processed, including smoothing with a Gaussian kernel with standard deviation of 50 px (Fig. 1d). The simulated ^{23}Na 1-channel ground truth was then multiplied with the sensitivity maps to obtain a multi-channel ^{23}Na ground truth (Fig. 1e). For each channel, the obtained Cartesian multi-channel ground truth was transformed into k-space. High frequencies were cut-off to obtain a nominal spatial resolution of $(3\,mm)^3$ (reconstructed to $(2.5\,mm)^3$ via zero filling). Subsequently, the Cartesian data set was regridded to a radial trajectory via a Kaiser-Bessel convolution kernel [39]. The biexponential T_2^* decay of sodium signal in the breast was simulated by multiplying the k-space projection-wise with

$$S_{dec}(t) = r \cdot e^{-\frac{t}{T_{2,s}^*}} + (1 - r) \cdot e^{-\frac{t}{T_{2,l}^*}}, \quad (8)$$

where following relaxation parameters were assumed: $r = 0.53$, $T_{2,s}^* = 2$ ms, $T_{2,l}^* = 17$ ms [41,42]. Finally, synthetic complex Gaussian noise was added to each projection. The noise was correlated based on a measured noise covariance matrix. This was done by decomposing the

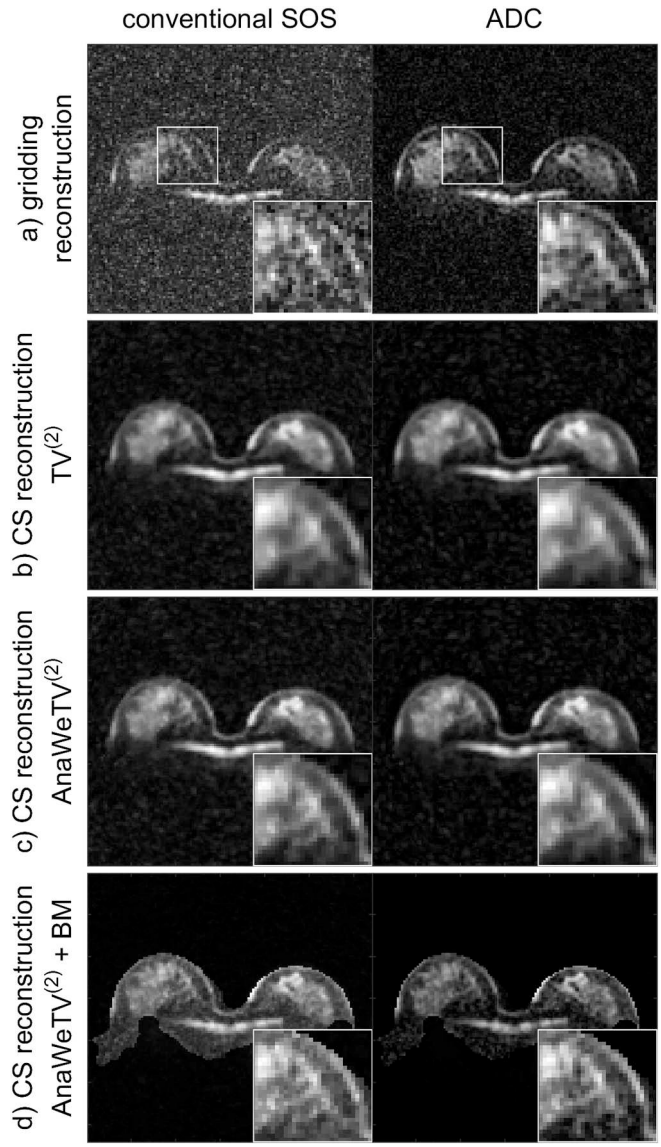

Fig. 6. Two different multi-channel combination methods (SOS and ADC) for the measured data set with 5000 projections (USF = 7.2) without raw data averaging (images from 32 years old healthy volunteer). a) Conventional gridding reconstruction versus CS reconstruction with a $TV^{(2)}$ (b) and an $AnaWeTV^{(2)}$ (c) as sparsity transformation and an additional BM constraint (d). The measurement confirms the results of the simulation: for the gridding reconstruction the ADC performs superior and shows a clear improvement compared to a simple SOS reconstruction. For the CS reconstruction, the different channel combination methods have distinctly less influence. The $AnaWeTV^{(2)}$ (with and without an additional BM) compared with the ADC gridding reconstruction shows an improved image quality (right column).

covariance matrix in an upper and lower triangular matrix; the lower triangular matrix was then used to correlate the originally normally distributed noise by multiplication. This follows the procedure described in the SENSE algorithm [43]. In this way, it is possible to simulate any data set with a specified correlated noise and different USFs (Fig. 1f). The corresponding SOS combination of the simulated multi-channel breast data set is shown in Fig. 1g. The workflow of the simulation scheme is shown in Fig. 1 for one slice and 4 (out of 14) selected simulated channels.

For the simulation study, the simulation parameters as well as the noise properties (i.e. noise level and noise correlation between the channels) were chosen to match the in vivo measurement. To examine the impact of changed noise properties, the noise level was increased/decreased by 20% with respect to the noise level matching the in vivo measurement; the noise correlation between the channels was changed reflecting weaker and stronger correlation (see Supplementary Fig. A.4). The data sets were reconstructed with the optimized weighting factors (see Supplementary Figs. A.1 and A.2).

2.4. In vivo measurements

In vivo MRI measurements of three female healthy subjects (28, 29 and 32 years old) were carried out at a 7 T whole-body system with a 70 mT/m gradient amplitude and a 200 mT/m/ms slew rate (Magnetom 7 T, Siemens Healthcare, Erlangen, Germany) by using prone patient positioning. The institutional review board approved this study and written informed consent was obtained. ^{23}Na as well as the Dixon ^{1}H MR measurements were acquired using a dual-tuned proton/sodium (^{1}H/^{23}Na) bilateral phased-array breast coil (14 ^{23}Na receive channels – of these, six were receive only, plus one transmit and receive channel per side, and two ^{1}H channels; QED, Mayfield Village, Ohio). A density adapted 3D radial projection reconstruction pulse sequence (DA-3DPR) [15] was employed with the following parameters: TR = 30 ms, TE = 0.55 ms, FA = 67°, nominal resolution: $(3\,\text{mm})^3$, reconstructed to $(2.5\,\text{mm})^3$ via zero filling, FOV: $(320\,\text{mm})^3$, T_{RO} = 9.98 ms. A noise scan to determine noise correlations and four ^{23}Na MR measurements with different USFs were carried out. The number of averages was adjusted to keep the total acquisition time constant (T_{AQ} = 600 s):

- USF = 1.8: 20000 projections/1 average,
- USF = 3.6: 10000 projections/2 averages,
- USF = 7.2: 5000 projections/4 averages,
- USF = 14.4: 2500 projections/8 averages.

The stated USFs were calculated with respect to the maximal necessary number of projections $N_{proj} = 4\pi\left(\frac{FOV/Res}{2}\right)^2 \approx 36000$ to fulfill the Nyquist criterion on the surface of the k-space sphere. The Nyquist theorem in radial direction was fulfilled with 384 samples per projection. The registered Dixon water and fat images were used to create a ^{23}Na ground truth (from which the simulated data sets are built up; see Section 2.3) and to obtain anatomical prior information (i.e. the BM and the weighting factors W_a; see Section 2.1).

2.5. Image assessment and optimization

The structural similarity (SSIM) [44] of an image x was calculated with respect to the reference ground truth r (combined Fig. 1e) and was used to assess the reconstruction of simulated data sets and to optimize the weighting factors τ_i [see Eq. (7)]. By calculating mean μ_x, standard deviation σ_x and correlation coefficient $\sigma_{xr} = \frac{1}{N-1}\sum_{i=1}^{N}(x_i - \mu_x)(r_i - \mu_r)$, luminance $l(x,r)$, contrast $c(x,r)$ and structure $s(x,r)$ terms are determined:

$$l(x,r) = \frac{2\mu_x\mu_r + C_1}{\mu_x^2 + \mu_r^2 + C_1}, \tag{9.1}$$

$$c(x,r) = \frac{2\sigma_x\sigma_r + C_2}{\sigma_x^2 + \sigma_r^2 + C_2}, \tag{9.2}$$

$$s(x,r) = \frac{\sigma_{xr} + C_3}{\sigma_x\sigma_r + C_3}. \tag{9.3}$$

As described in [44], the constants $C_1 = 1\cdot10^{-4}$, $C_2 = 9\cdot10^{-4}$ and $C_3 = \frac{C_2}{2}$ were used to avoid instability in case of denominators close to zero. The SSIM was calculated by combining all three terms to one measure:

$$SSIM(x,r) = l(x,r)\cdot c(x,r)\cdot s(x,r). \tag{10}$$

The default values for the Gaussian kernel (filtersize: 11 px,

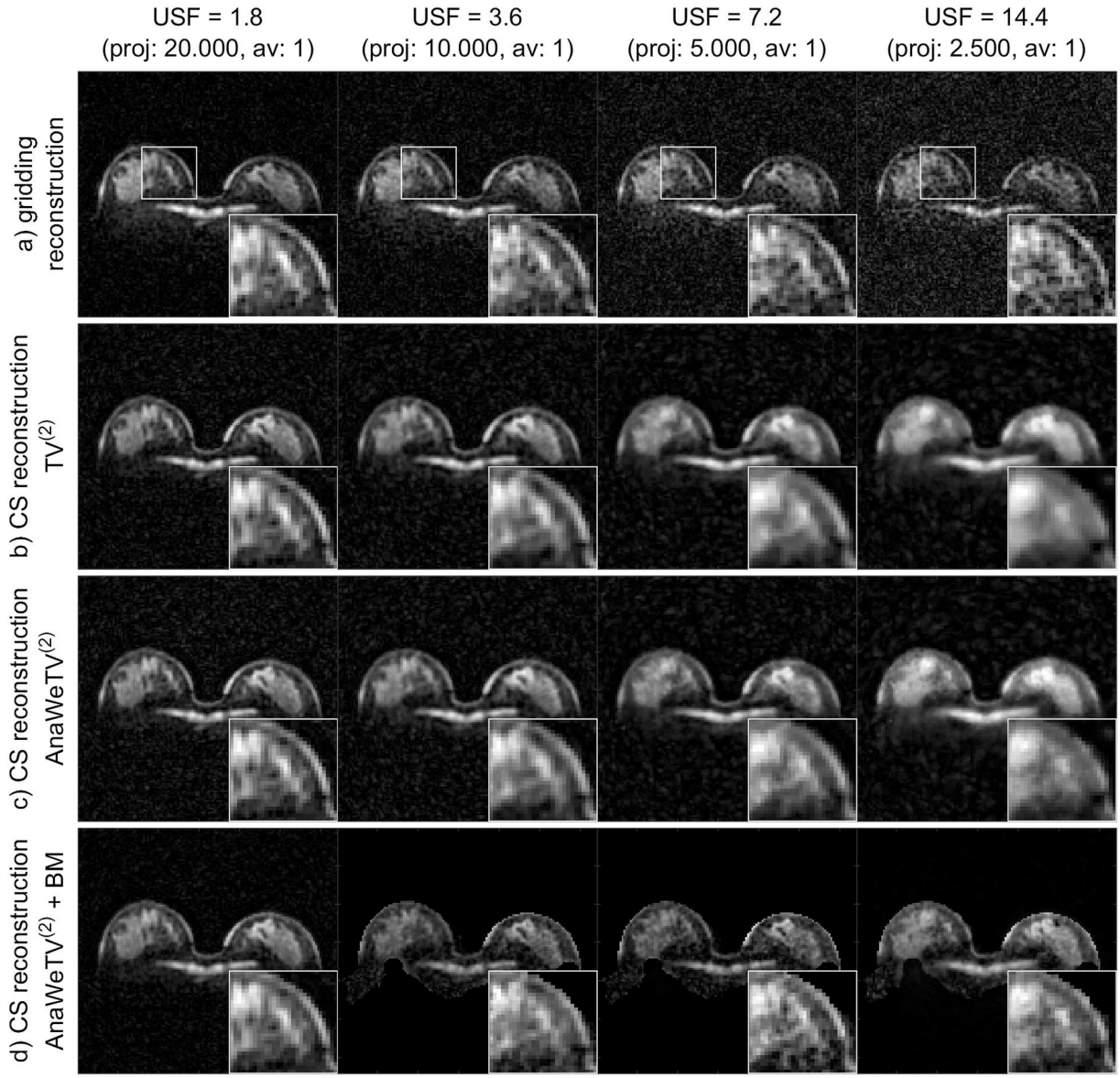

Fig. 7. Reconstruction of measured multi-channel breast data with different USFs without raw data averaging, combined via ADC (images from 32 years old healthy volunteer). a) Conventional gridding reconstruction versus CS reconstruction with a $TV^{(2)}$ (b) and an $AnaWeTV^{(2)}$ (c) as sparsity transformation and an additional BM constraint (d). The $AnaWeTV^{(2)}$ leads to an improved image quality compared to the gridding reconstruction, especially for high USFs. An additional BM shows further improvements only for higher USFs (USF = 7.2/14.4).

standard deviation: 1.5 px) [44] were used to weight neighboring pixels and avoid blocking-like artifacts. In addition, the SSIM values were calculated only inside the object, identified via a BM and averaged over the 3D data set. A value of 1 corresponds to complete agreement between the reference r and the reconstructed image x.

To optimize the weighting factor $\tau_{TV^{(2)}}$ for the $TV^{(2)}$ sparsity transformation [see Eq. (7.1)], the simulated data set was reconstructed with different values for $\tau_{TV^{(2)}}$ in the range between $5{\cdot}10^{-5}$ and $1.5{\cdot}10^{-2}$; the ADC combined image was then assessed using the SSIM (see Supplementary Fig. A.1). The $\tau_{TV^{(2)}}$ value with the highest resulting SSIM value was determined for each USF and used likewise for $\tau_{AnaWeTV^{(2)}}$ [see Eq. (7.2)]. Keeping the optimized $\tau_{AnaWeTV^{(2)}}$ value constant, τ_{BM} was varied in the range of 0.5 and 50 and the SSIM values of the corresponding images were assessed again (see Supplementary Fig. A.2). This optimization process was done for each individual in vivo measurement by creating and assessing corresponding simulated data sets. The optimized weighting factors τ_i were then transferred to the CS reconstruction of in vivo data.

To assess quantitative changes of the image intensity between the different reconstruction methods and USFs, the signal ratio between the water and fat region (i.e. between the glandular and adipose breast tissue) was calculated. The corresponding regions were identified via the water and fat binary masks, the mean intensity inside the masks and from that the signal ratio between glandular and adipose tissue was calculated.

Four additional data sets with differently randomly distributed noise were simulated and reconstructed using the ADC optimized weighting factors for data set a). For the SSIM value and the signal ratio, mean and standard deviation of the five data sets were calculated for each reconstruction method and USF.

3. Results

3.1. Simulation results

Two different combination methods were analyzed for the simulated data set with 5000 projections (USF = 7.2) (Fig. 2). For the

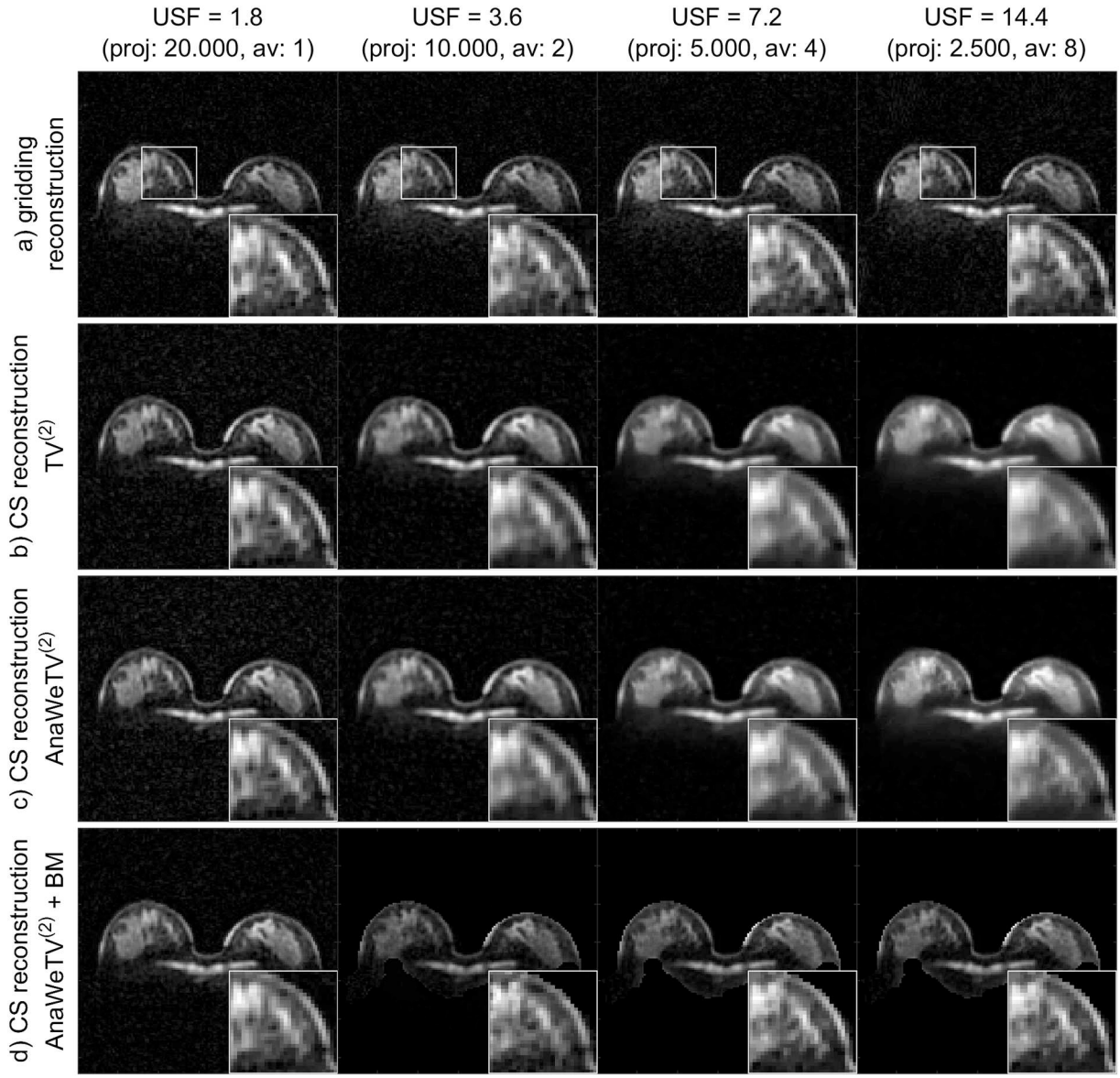

Fig. 8. Reconstruction of measured multi-channel breast data with different USFs and raw data averaging, combined via ADC (images from 32 years old healthy volunteer). The number of averages was adjusted to keep the total acquisition time constant for different USFs. a) Conventional gridding reconstruction versus CS reconstruction with a $TV^{(2)}$ (b) and an $AnaWeTV^{(2)}$ (c) as sparsity transformation and an additional BM constraint (d). The measurement confirms the simulation: the decline in image quality with higher USFs, using a $TV^{(2)}$ and $AnaWeTV^{(2)}$ CS reconstruction, is less pronounced compared to non-averaged raw data in Fig. 7. By incorporating an additional BM into the reconstruction the image quality is similar for all USFs.

gridding reconstruction, the ADC shows a clear reduction of the background signal compared with the conventional SOS combination and increases the image quality markedly (Fig. 2a). For the CS reconstructions, the ADC also improves the results compared to a simple SOS combination. However, the improvements are less distinct, especially for the conventional $TV^{(2)}$ CS reconstruction; the $AnaWeTV^{(2)}$ + BM reconstruction profits most from an ADC combination (Fig. 2b,c,d). The $AnaWeTV^{(2)}$ reconstruction yields an improvement compared to the $TV^{(2)}$ reconstruction due to the preserving of known tissue boundaries. Accordingly, the $AnaWeTV^{(2)}$ CS reconstruction yields higher SSIM values. A BM as further regularization shows additional improvements. Comparing the ADC combination for the gridding and the CS reconstruction, the use of the $AnaWeTV^{(2)}$ sparsity transformation with and without an additional BM shows higher SSIM values than the conventional gridding reconstruction (Fig. 2, right column). For the conventional gridding and the CS reconstruction, the ratio can be increased using ADC (Fig. 2). For the $AnaWeTV^{(2)}$ and $AnaWeTV^{(2)}$ + BM reconstructions, the ratios are increased compared to the conventional $TV^{(2)}$ reconstruction and exceed those of the ADC gridding reconstruction. The $AnaWeTV^{(2)}$ + BM reconstruction shows the highest ratio (Fig. 2, right column).

If ADC is applied, the gridding reconstruction performs similar compared to the $TV^{(2)}$ CS reconstruction (Fig. 3a,b). The $AnaWeTV^{(2)}$ reconstruction (Fig. 3c) shows improved SSIM values compared to the gridding reconstruction (Fig. 3a) and exceed those, especially for higher USFs. For the higher USFs (USF = 7.2/14.4), an additional BM shows further improvements (Fig. 3d) and increase the image quality markedly. The SSIM values indicate that despite high USFs (e.g. USF = 7.2, i.e. 4-fold reduced acquisition time) the quality of the $AnaWeTV^{(2)}$ + BM reconstructed image is only slightly reduced compared to the ADC gridding reconstruction of the highly sampled data set (USF = 1.8). For all reconstructions, the signal ratio glandular/adipose decreases with increasing USF (Fig. 3). Using the $AnaWeTV^{(2)}$ reconstruction, the ratios are similar for an USF = 1.8 and increased for

USF = 3.6/7.2/14.4 compared to the $TV^{(2)}$ reconstruction; for the higher USFs an additionally included BM increases the ratio further. Using the $AnaWeTV^{(2)}$ + BM reconstruction, the ratios exceed those of the ADC gridding reconstruction for all USFs (Fig. 3a,d). The $TV^{(2)}$ and $AnaWeTV^{(2)}$ reconstructions for an USF of 1.8 show the highest ratio.

For the data set with USF = 7.2, the performance of the conventional gridding reconstruction and the CS reconstructions were analyzed for varied noise properties (Fig. 4). With respect to the reconstructed data set matching the in vivo measurement (Fig. 3, second column from the right), the SSIM values are lower for the data set with raised noise level and higher for the data set with decreased noise level (Fig. 4, two left columns); stronger/weaker noise correlations between the channels lead to slightly lower/higher SSIM values (Fig. 4, two right columns). For all four different assumed noise properties, the $AnaWeTV^{(2)}$ and $AnaWeTV^{(2)}$ + BM reconstructions perform superior compared to the conventional ADC gridding reconstruction; the $AnaWeTV^{(2)}$ + BM reconstruction shows always the best performance indicated by the highest SSIM values and ratios.

For the ADC gridding reconstruction, undersampling with corresponding raw data averaging (i.e. same total measurement time, despite lower USFs) yields a decrease of the SSIM values with increasing USF (Fig. 5a). The decrease is distinctly lower compared to non-averaged raw data (Fig. 3a). The same applies to the $TV^{(2)}$ and $AnaWeTV^{(2)}$ CS reconstructions (Fig. 5b,c). If the BM is included, the image quality is increased especially for high USFs and gets similar for all USFs (Fig. 5d). The ratio glandular/adipose decreases with increasing USFs for all reconstructions (Fig. 5). However, the decline is less strong compared to non-averaged raw data sets. The $AnaWeTV^{(2)}$ reconstruction increases the ratio compared to the $TV^{(2)}$ reconstruction for USF = 3.6/7.2/14.4; an additionally included BM increases the ratio further for USF = 7.2/14.4. The ratio for the $AnaWeTV^{(2)}$ + BM reconstruction exceed those of the gridding reconstruction for all USFs (Fig. 5a,d).

3.2. In vivo measurements

In the same way as for the simulated data (Fig. 2), measured data were reconstructed and combined using the implemented methods (Fig. 6). The results from in vivo measurements are in agreement with the findings of the simulation study. For the gridding reconstruction, the ADC combination shows a better performance and image quality is improved compared to a conventional SOS combination (Fig. 6a). For the $TV^{(2)}$ and $AnaWeTV^{(2)}$ CS reconstruction, no distinct differences between SOS and ADC are noticeable (Fig. 6b,c); the $AnaWeTV^{(2)}$ + BM reconstruction profits from the ADC combination (Fig. 6d).

The reconstruction of measured data combined via ADC for different USFs (Fig. 7) confirms the simulation as well (Fig. 3). Compared to the gridding reconstruction the CS reconstruction leads to a reduction of the background signal, especially for high USFs, where noise and undersampling artifacts are more pronounced. The $AnaWeTV^{(2)}$ reconstruction (Fig. 7c) shows a reduced blurring compared to the $TV^{(2)}$ reconstruction (Fig. 7b). In particular for high USFs, improvements due to an additional BM regularization are visible (Fig. 7d).

The averaged, gridding reconstructed in vivo data shows barely changed image quality for the different USFs (Fig. 8a). For the CS reconstructions with a $TV^{(2)}$ and $AnaWeTV^{(2)}$ sparsity transformation, a slight decrease in image quality is noticeable (Fig. 8b,c); however, this decline is less pronounced compared to non-averaged raw data (Fig. 7). By incorporating an additional BM, image quality is again similar for all USFs (Fig. 8d). This is in agreement with the simulation study (Fig. 5).

4. Discussion

We analyzed an iterative image reconstruction method based on CS for ^{23}Na multi-channel data sets. A $TV^{(2)}$ as sparsity transformation for a CS reconstruction is utilized as a denoising technique to reduce noise and incoherent undersampling artifacts. Since the $TV^{(2)}$ reconstruction inevitable leads to image blurring, the $TV^{(2)}$ reconstruction is adopted such that the denoising is less strong at known tissue boundaries ($AnaWeTV^{(2)}$). Thus, even fine structure can be resolved, while noise is reduced and partial volume effects are diminished. For the lowest USFs of 1.8 and 3.6, a binary mask as additional regularization leads to negligible additional improvements of image quality. However, for higher USFs (of 7.2 and 14.4) the image quality profits clearly from the incorporated BM.

For a conventional gridding reconstruction, sophisticated channel combination methods, such as ADC, markedly improve the image quality [31,32]. For the presented CS reconstruction a simple SOS combination results only in a slightly reduced image quality compared to ADC, especially for the conventional $TV^{(2)}$ CS reconstruction. This is most likely caused by the reduced noise of the CS reconstructed images, since for high SNR data even a SOS combination shows optimal results [45]. An additional noise scan and the optimization of the ADC reconstruction by choosing a suitable block and interpolation size is then not required. Note that the performance of the ADC algorithm also depends on the strength of the noise correlations between the channels. Thus, results for other coils might differ.

Comparing the ADC gridding reconstruction as state-of-the-art for low SNR sodium imaging with the $AnaWeTV^{(2)}$ CS reconstruction with and without an additional BM, the results indicate that the CS reconstruction shows its benefits in particular for low USFs of 7.2 and 14.4 (see Supplementary Fig. A.3). Therefore, the reconstruction time can be reduced (e.g. 4-fold to an USF = 7.2), while the image quality is only slightly worse compared to an almost fully sampled (USF = 1.8) gridding reconstructed data set. Furthermore, these results are generalizable to varying noise conditions, i.e. different randomly distributed noise, noise levels and noise correlations.

Both simulated and measured data sets confirm these results. However, for the evaluation of nonlinear CS reconstructed images no gold standard exists. The SNR cannot be reliably calculated and the point spread function is locally dependent and difficult to determine. For Cartesian CS a method was proposed by Wech et al. [46]. However, it can't be easily transferred to 3D radial CS. The simulation has the decisive advantage of an existing ground truth, which serves as reference and can be used to assess the reconstructed images via SSIM and to optimize the weighting factors; for in vivo data this is not possible.

To the best of our knowledge, this is the first time CS has been applied to a multi-channel ^{23}Na data set. The results are in accordance with a previous study that used 1-channel ^{23}Na MRI head data [29]. Our work demonstrates benefits of the $AnaWeTV^{(2)}$ sparsity transformation for the CS reconstruction of 14-channel ^{23}Na MRI data by preserving known tissue boundaries and reducing partial volume and undersampling effects. The algorithm takes advantages of CS [25] and in particular of a $TV^{(2)}$ sparsity transformation instead of a $TV^{(1)}$ [37]. While the incorporation of ^{1}H prior information into the $TV^{(2)}$ only requires a registration of the ^{1}H and the ^{23}Na image, other algorithms are based on image segmentation [47,48], which might be more time-consuming. Previous work showed for dictionary learning compressed sensing a clear benefit for undersampled and averaged raw data compared to a fully sampled data set with the same total measurement time [26]. In contrast, for the here applied multi-channel $TV^{(2)}$ and $AnaWeTV^{(2)}$ reconstruction the image quality of an almost fully sampled data set (USF = 1.8) is always superior compared to undersampled and averaged image data (see Supplementary Fig. A.3, right column). For the $AnaWeTV^{(2)}$ + BM reconstruction image quality is similar and in some cases slightly better compared to a nearly fully sampled data set. This can be explained by the more distinct undersampling artifacts at higher USFs of 7.2 and 14.4. An additionally included BM leads to larger improvements in image quality compared to low USFs of 1.8 and 3.6 and image quality gets comparable for all USFs. However, a clear trend for all three data sets that the presented reconstruction can distinctly profit from averaged raw data can't be comprehended (see

Supplementary Fig. A.3, right column). This might be caused by the small local FOVs of the receive elements.

It should be noted that the AnaWeTV$^{(2)}$ reconstruction does not falsify the ^{23}Na reconstruction, since it only reduce the denoising property of the TV$^{(2)}$ at known tissue boundaries. Thus, no signal intensity is transferred from the ^{1}H image to the ^{23}Na image. In the case of novel pathologies (e.g. small lesions) that are visible only in ^{23}Na MRI, the AnaWeTV$^{(2)}$ reconstruction does not improve the detectability. The reconstruction is then similar to a conventional TV$^{(2)}$ reconstruction.

In contrast to the conventional gridding reconstruction, the presented CS algorithm requires longer reconstruction time and higher computational power in particular to reconstruct (fully-sampled) data sets. For measured data no ground truth exists, which is a requirement for the calculation of the SSIM values. Thus, the optimized weighting factors obtained from the simulation studies were directly transferred to reconstruct the corresponding measured data sets. This approach seems to be valid, since general weighting factors ($\tau_{\mathrm{TV}^{(2)}} = \tau_{\mathrm{AnaWeTV}^{(2)}} = 0.0025$ and $\tau_{\mathrm{BM}} = 2$) can be used, which lead to almost optimal SSIM values for all USFs, averaged and non-averaged raw data and the three different data sets (see Supplementary Figs. A.1 and A.2). However, simulated data sets are based on a water and a fat binary mask, which are created by thresholding. Potential variations of the sodium concentration within the masks are neglected. Therefore, simulations and in vivo measurements do not coincide entirely and the optimal weighting factors for simulated and measured data might differ. Since the optimized weighting factors for the CS reconstructions are similar for different breast data sets, the omission of potential variations seems to be valid. Moreover, the determined weighting factors lead to high-quality images also for measured data. Furthermore, this approach enables statements about possible quantitative changes for each reconstruction and USF. The weighting between the first and second order derivative ($\lambda = 0.77$) was chosen according to Block et al. [36], referring to 1-channel data sets. Since individually CS reconstructed single-channel data sets are combined, this seems to be a valid choice for the here presented algorithm, too. However, there might be even better weighting factors λ for the CS reconstruction of multi-channel data sets. Beyond that corrections of transmit and receive profiles are required for future quantitative measurements.

5. Conclusion

In this work, a CS based reconstruction algorithm for ^{23}Na multi-channel data sets is presented. The TV$^{(2)}$ as sparsity transformation was adapted by weighting factors (AnaWeTV$^{(2)}$) such that noise and (undersampling) artifacts are suppressed, while known tissue boundaries are preserved. Additionally, a support region (BM), which matches the object shape, was included into the reconstruction to penalize intensities outside of the object. The proposed reconstructions were tested on simulated data as well as in vivo breast measurements at 7 T. For high USFs (USF = 7.2/14.4), the AnaWeTV$^{(2)}$ + BM CS reconstruction yielded higher SSIM values for the three analyzed data sets – indicating improved image quality – when compared to a conventional ADC gridding reconstruction. Therefore, the proposed algorithm can be used to reduce the total acquisition time, while preserving image quality.

Supplementary data to this article can be found online at https://doi.org/10.1016/j.mri.2019.03.024.

Funding

This work was supported by the Vienna Science and Technology Fund (WWTF, project LS14-096).

Declarations of interest

None.

References

[1] Thulborn KR, Davis D, Snyder J, Yonas H, Kassam A. Sodium MR imaging of acute and subacute stroke for assessment of tissue viability. Neuroimaging Clin N Am 2005;15(3):639–53. xi-xii https://doi.org/10.1016/j.nic.2005.08.003.
[2] Tsang A, Stobbe RW, Asdaghi N, Hussain MS, Bhagat YA, Beaulieu C, et al. Relationship between sodium intensity and perfusion deficits in acute ischemic stroke. J Magn Reson Imaging 2011;33(1):41–7. https://doi.org/10.1002/jmri.22299.
[3] Inglese M, Madelin G, Oesingmann N, Babb JS, Wu W, Stoeckel B, et al. Brain tissue sodium concentration in multiple sclerosis: a sodium imaging study at 3 tesla. Brain 2010;133(3):847–57. https://doi.org/10.1093/brain/awp334.
[4] Petracca M, Fleysher L, Oesingmann N, Inglese M. Sodium MRI of multiple sclerosis. NMR Biomed 2016;29(2):153–61. https://doi.org/10.1002/nbm.3289.
[5] Zaaraoui W, Konstandin S, Audoin B, Nagel AM, Rico A, Malikova I, et al. Distribution of brain sodium accumulation correlates with disability in multiple sclerosis: a cross-sectional 23Na MR imaging study. Radiology 2012;264(3):859–67. https://doi.org/10.1148/radiol.12112680.
[6] Goldsmith M, Damadian R. NMR in cancer. VII. Sodium-23 magnetic resonance of normal and cancerous tissues. Physiol Chem Phys 1975;7(3):263–9.
[7] Schepkin VD. Sodium MRI of glioma in animal models at ultrahigh magnetic fields. NMR Biomed 2016;29(2):175–86. https://doi.org/10.1002/nbm.3347.
[8] Jacobs MA, Ouwerkerk R, Wolff AC, Stearns V, Bottomley PA, Barker PB, et al. Multiparametric and multinuclear magnetic resonance imaging of human breast cancer: current applications. Technol Cancer Res Treat 2004;3(6):543–50. https://doi.org/10.1177/153303460400300603.
[9] Ouwerkerk R, Jacobs MA, Macura KJ, Wolff AC, Stearns V, Mezban SD, et al. Elevated tissue sodium concentration in malignant breast lesions detected with non-invasive 23Na MRI. Breast Cancer Res Treat 2007;106(2):151–60. https://doi.org/10.1007/s10549-006-9485-4.
[10] Zaric O, Pinker K, Zbyn S, Strasser B, Robinson S, Minarikova L, et al. Quantitative sodium MR imaging at 7 T: initial results and comparison with diffusion-weighted imaging in patients with breast tumors. Radiology 2016;280(1):39–48. https://doi.org/10.1148/radiol.2016151304.
[11] Madelin G, Regatte RR. Biomedical applications of sodium MRI in vivo. J Magn Reson Imaging 2013;38(3):511–29. https://doi.org/10.1002/jmri.24168.
[12] Thulborn KR. Quantitative sodium MR imaging: a review of its evolving role in medicine. Neuroimage 2018;168:250–68. https://doi.org/10.1016/j.neuroimage.2016.11.056.
[13] Ladd ME, Bachert P, Meyerspeer M, Moser E, Nagel AM, Norris DG, et al. Pros and cons of ultra-high-field MRI/MRS for human application. Prog Nucl Magn Reson Spectrosc 2018;109:1–50. https://doi.org/10.1016/J.PNMRS.2018.06.001.
[14] Konstandin S, Nagel AM. Measurement techniques for magnetic resonance imaging of fast relaxing nuclei. MAGMA 2014;27(1):5–19. https://doi.org/10.1007/s10334-013-0394-3.
[15] Nagel AM, Laun FB, Weber MA, Matthies C, Semmler W, Schad LR. Sodium MRI using a density-adapted 3D radial acquisition technique. Magn Reson Med 2009;62(6):1565–73. https://doi.org/10.1002/mrm.22157.
[16] Star-Lack J, Roos M, Wong S, Schepkin V, Budinger T. Four-dimensional 1H and 23Na imaging using continuously oscillating gradients. J Magn Reson 1997;124(2):420–38. https://doi.org/10.1006/jmre.1996.1052.
[17] Gurney PT, Hargreaves BA, Nishimura DG. Design and analysis of a practical 3D cones trajectory. Magn Reson Med 2006;55(3):575–82. https://doi.org/10.1002/mrm.20796.
[18] Boada FE, Gillen JS, Shen GX, Chang SY, Thulborn KR. Fast three dimensional sodium imaging. Magn Reson Med 1997;37(5):706–15. https://doi.org/10.1002/mrm.1910370512.
[19] Lu A, Atkinson IC, Claiborne TC, Damen FC, Thulborn KR. Quantitative sodium imaging with a flexible twisted projection pulse sequence. Magn Reson Med 2010;63(6):1583–93. https://doi.org/10.1002/mrm.22381.
[20] Pipe JG, Zwart NR, Aboussouan EA, Robison RK, Devaraj A, Johnson KO. A new design and rationale for 3D orthogonally oversampled k-space trajectories. Magn Reson Med 2011;66(5):1303–11. https://doi.org/10.1002/mrm.22918.
[21] Bottomley PA. Sodium MRI in man: technique and findings. eMagRes 2012;1:353–66. https://doi.org/10.1002/9780470034590.emrstm1252.
[22] Bangerter NK, Kaggie JD, Taylor MD, Hadley JR. Sodium MRI radiofrequency coils for body imaging. NMR Biomed 2016;29(2):107–18. https://doi.org/10.1002/nbm.3392.
[23] Kaggie JD, Hadley JR, Badal J, Campbell JR, Park DJ, Parker DL, et al. A 3 T sodium and proton composite array breast coil. Magn Reson Med 2014;71(6):2231–42. https://doi.org/10.1002/mrm.24860.
[24] Wiggins GC, Brown R, Lakshmanan K. High-performance radiofrequency coils for 23Na MRI: brain and musculoskeletal applications. NMR Biomed 2016;29(2):96–106. https://doi.org/10.1002/nbm.3379.
[25] Lustig M, Donoho D, Pauly JM. Sparse MRI: the application of compressed sensing for rapid MR imaging. Magn Reson Med 2007;58(6):1182–95. https://doi.org/10.1002/mrm.21391.
[26] Behl NG, Gnahm C, Bachert P, Ladd ME, Nagel AM. Three-dimensional dictionary-learning reconstruction of 23Na MRI data. Magn Reson Med 2016;75(4):1605–16. https://doi.org/10.1002/mrm.25759.
[27] Gnahm C, Bock M, Bachert P, Semmler W, Behl NG, Nagel AM. Iterative 3D projection reconstruction of 23Na data with an 1H MRI constraint. Magn Reson Med 2014;71(5):1720–32. https://doi.org/10.1002/mrm.24827.
[28] Madelin G, Chang G, Otazo R, Jerschow A, Regatte RR. Compressed sensing sodium MRI of cartilage at 7T: preliminary study. J Magn Reson 2012;214:360–5. https://

doi.org/10.1016/j.jmr.2011.12.005.
[29] Gnahm C, Nagel AM. Anatomically weighted second-order total variation reconstruction of 23Na MRI using prior information from 1H MRI. Neuroimage 2015;105:452–61. https://doi.org/10.1016/j.neuroimage.2014.11.006.
[30] Roemer PB, Edelstein WA, Hayes CE, Souza SP, Mueller OM. The NMR phased array. Magn Reson Med 1990;16(2):192–225. https://doi.org/10.1002/mrm.1910160203.
[31] Walsh DO, Gmitro AF, Marcellin MW. Adaptive reconstruction of phased array MR imagery. Magn Reson Med 2000;43(5):682–90. https://doi.org/10.1002/(SICI)1522-2594(200005)43:5%3C682::AID-MRM10%3E3.0.CO;2-G.
[32] Benkhedah N, Hoffmann SH, Biller A, Nagel AM. Evaluation of adaptive combination of 30-channel head receive coil array data in 23Na MR imaging. Magn Reson Med 2016;75(2):527–36. https://doi.org/10.1002/mrm.25572.
[33] Pruessmann KP, Weiger M, Scheidegger MB, Boesiger P. SENSE: sensitivity encoding for fast MRI. Magn Reson Med 1999;42(5):952–62. https://doi.org/10.1002/(SICI)1522-2594(199911)42:5%3C952::AID-MRM16%3E3.0.CO;2-S.
[34] Qian Y, Zhao T, Wiggins GC, Wald LL, Zheng H, Weimer J, et al. Sodium imaging of human brain at 7 T with 15-channel array coil. Magn Reson Med 2012;68(6):1807–14. https://doi.org/10.1002/mrm.24192.
[35] Weingärtner S, Wetterling F, Konstandin S, Fatar M, Neumaier-Probst E, Schad LR. Scan time reduction in 23Na-magnetic resonance imaging using the chemical shift imaging sequence: evaluation of an iterative reconstruction method. Z Med Phys 2015;25(3):275–86. https://doi.org/10.1016/j.zemedi.2014.08.007.
[36] Block KT, Uecker M, Frahm J. Undersampled radial MRI with multiple coils. Iterative image reconstruction using a total variation constraint. Magn Reson Med 2007;57(6):1086–98. https://doi.org/10.1002/mrm.21236.
[37] Geman D, Yang C. Nonlinear image recovery with half-quadratic regularization. IEEE Trans Image Process 1995;4(7):932–46. https://doi.org/10.1109/83.392335.
[38] Zhang L, Zhou W, Li D-H. A descent modified Polak–Ribière–Polyak conjugate gradient method and its global convergence. IMAJNA 2006;26(4):629–40. https://doi.org/10.1093/imanum/drl016.
[39] Jackson JI, Meyer CH, Nishimura DG, Macovski A. Selection of a convolution function for Fourier inversion using gridding (computerised tomography application). IEEE Trans Med Imaging 1991;10(3):473–8. https://doi.org/10.1109/42.97598.
[40] Dagum L, Menon R. OpenMP: an industry standard API for shared-memory programming. IEEE Comput Sci Eng 1998;5(1):46–55. https://doi.org/10.1109/99.660313.
[41] Ianniello C, Madelin G, Lakshmanan K, Zhang B, Moy L, Brown R. Design and performance of a dual tuned 7 T proton/sodium breast coil. Paper presented at: international conference on electromagnetics in advanced applications 2017. https://doi.org/10.1109/ICEAA.2017.8065675. 11-15 Sept. Verona, IT.
[42] Zbyn S, Juras V, Benkhedah N, Zaric O, Mlynarik V, Szomolanyi P, et al. Bilateral in vivo mapping of sodium relaxation times in breasts at 7T. Paper presented at: annual meeting of the ISMRM. 2015. 30 May-5 June. [Toronto, Ontario, CAN].
[43] Pruessmann KP, Weiger M, Bornert P, Boesiger P. Advances in sensitivity encoding with arbitrary k-space trajectories. Magn Reson Med 2001;46(4):638–51. https://doi.org/10.1002/mrm.1241.
[44] Wang Z, Bovik AC, Sheikh HR, Simoncelli EP. Image quality assessment: from error visibility to structural similarity. IEEE Trans Image Process 2004;13(4):600–12. https://doi.org/10.1109/TIP.2003.819861.
[45] Larsson EG, Erdogmus D, Yan R, Principe JC, Fitzsimmons JR. SNR-optimality of sum-of-squares reconstruction for phased-array magnetic resonance imaging. J Magn Reson 2003;163(1):121–3. https://doi.org/10.1016/S1090-7807(03)00132-0.
[46] Wech T, Stäb D, Fischer A, Hahn D, Köstler H. On the quality evaluation for images reconstructed by compressed sensing. Paper presented at: annual meeting of the ISMRM. 2011. 7 - 13 May. [Montreal, Quebec, CAN].
[47] Eslami R, Jacob M. Robust reconstruction of MRSI data using a sparse spectral model and high resolution MRI priors. IEEE Trans Med Imaging 2010;29(6):1297–309. https://doi.org/10.1109/Tmi.2010.2046673.
[48] Haldar JP, Jacob M, Ebel A, Zhu X, Schuff N, Hernando D, et al. Regularized inversion of noisy, incomplete MR spectroscopic imaging data with anatomical prior. Paper presented at: 3rd IEEE international symposium on biomedical imaging: nano to macro 2006. https://doi.org/10.1109/ISBI.2006.1625017. 6-9 April. Arlington, VA, USA.